actuators

MDPI

Article

Rod-Shaped Linear Inertial Type Piezoelectric Actuator

Andrius Čeponis [1,*], Vytautas Jūrėnas [1], Dalius Mažeika [2], Vytautas Bakanauskas [3] and Dovilė Deltuvienė [4]

[1] Laboratory of Robotics and Piezomechanics, Institute of Mechatronics, Kaunas University of Technology, K. Donelaičio Str. 73, 44249 Kaunas, Lithuania; vytautas.jurenas@ktu.lt
[2] Department of Information Systems, Faculty of Fundamental Sciences, Vilnius Gediminas Technical University, Sauletekio Avn., 10223 Vilnius, Lithuania; dalius.mazeika@vilniustech.lt
[3] Department of Research and Development, Advanced Materials & Solutions, Prague Facility, CTS Corporation, 25101 Nupaky, Czech Republic; vytautas.bakanauskas@ctscorp.com
[4] Department of Mathematical Statistics, Faculty of Fundamental Sciences, Vilnius Gediminas Technical University, Sauletekio Avn., 10223 Vilnius, Lithuania; dovile.deltuviene@vilniustech.lt
* Correspondence: andrius.ceponis@ktu.lt

Abstract: This article presents a numerical and experimental investigation of a novel rod-shaped linear piezoelectric actuator that consists of a square cross-section-shaped rod with eight piezo ceramic plates and a cylindrical guidance rail. The rod has a hollow cut made with an offset from the longitudinal axis of the symmetry. A cylindrical guidance rail is placed on one side of the rod, while T-shaped clamping is formed on the opposite side. The slider is mounted on the rail and is moved along it. The actuator is compact, making it possible to mount it directly on a printed circuit board (PCB) or in another device with limited mounting space, restricted mass, or actuator footprint. The operation of the actuator is based on the excitation of the first longitudinal vibration mode of the rod that induces in-plane bending vibration of the nodal zone of the rod due to a hollowed cut asymmetrically placed in the central part of the actuator. The actuator is driven by two sawtooth waveform electric signals with the phase difference of π that allows exciting longitudinal deformations of the rod and controls the reverse motion of the slider. The results of numerical investigations confirmed the operation principle of the actuator at the frequency of 59.72 kHz. The maximum displacement amplitude of the guidance rail in the longitudinal direction reaches up to 152.9 µm while the voltage of 200 $V_{p\text{-}p}$ was applied. An experimental investigation of the actuator was made, and a maximum linear speed of 45.6 mm/s and thrust force of 115.4 mN was achieved.

Keywords: linear piezoelectric actuator; square rod stator; longitudinal deformation mode; inertial actuator

check for updates

Citation: Čeponis, A.; Jūrėnas, V.; Mažeika, D.; Bakanauskas, V.; Deltuvienė, D. Rod-Shaped Linear Inertial Type Piezoelectric Actuator. *Actuators* **2023**, *12*, 379. https://doi.org/10.3390/act12100379

Academic Editor: Katsushi Furutani

Received: 15 September 2023
Revised: 30 September 2023
Accepted: 6 October 2023
Published: 7 October 2023

Copyright: © 2023 by the authors. Licensee MDPI, Basel, Switzerland. This article is an open access article distributed under the terms and conditions of the Creative Commons Attribution (CC BY) license (https://creativecommons.org/licenses/by/4.0/).

1. Introduction

Modern research and manufacturing systems, environment scanning systems, and micro/nano satellites rely on high-accuracy optical and laser systems. These systems create a demand for high-accuracy motors and actuators [1,2]. Moreover, additional requirements, such as small mass, limited footprint area or mounting space, as well as flexible driving and mounting options, are applied for such motors and actuators [3,4]. Usually, electromagnetic motors and actuators are used for optical and laser systems. However, electromagnetic drives have drawbacks, such as electromagnetic interference with electronic devices that affect their application option close to sensitive electronics. Also, the scalability of electromagnetic motors and actuators is limited because of the manufacturing and technological aspects. In most cases, electromagnetic motors and actuators cannot drive the payload directly; therefore, a transmission system is needed which increases the mass of the whole electro-mechanical system [5–7].

To address these drawbacks and limitations effectively, alternative sources of motion must be introduced and utilized.

Piezoelectric drives emerge as the most promising alternative to replace electromagnetic motion actuators and motors in high-precision motion systems [8]. Piezoelectric motors and actuators have good scalability and operate without magnetic fields, enabling them to achieve nano or micro-level motion resolution without the need for transmission or additional support systems. Moreover, piezoelectric drives possess a self-locking capability without any power consumption and can meet strict requirements of footprints, mass, and mounting space [9–13]. Furthermore, piezoelectric actuators and motors can be designed as multipurpose drives that provide several degrees of freedom and generate rotary and linear motion of the payload using a single actuator [14,15]. However, it must be noted that multi-degree-of-freedom piezoelectric actuators have main drawbacks, such as a more complex design compared to single-degree-of-freedom actuators [16,17].

Piezoelectric actuators can be classified based on their operational principles into the following categories: traveling wave, inchworm, and inertial actuators [18]. Although traveling wave and inchworm-type actuators have certain advantages, inertial actuators are the most commonly employed method for achieving linear load motion. This preference is attributed to its simplicity of excitation and its ability to attain high motion resolutions, rapid motion speeds, and small response times [19,20]. While there are notable advantages of already developed inertial linear motion actuators, there continues to be a demand for piezoelectric inertial linear motion actuators that are characterized by simple design, small size and volume, flexible driving, and mounting.

Lu et al. introduced an inertial linear piezoelectric actuator based on an asymmetric flexure hinge with a triangular displacement amplification mechanism driven by a multilayer piezoelectric actuator [21]. The operation of the actuator is based on low-frequency longitudinal displacements of the multilayer piezoelectric actuator, which are inducted by the sawtooth electric signal. The longitudinal displacements of the actuator generate bending vibrations of the whole stator because of the asymmetry of the hinges and are amplified by a mechanical amplification mechanism. The actuator operates based on the slick-stick operation principle when a sawtooth waveform excitation signal is applied. Motion is transferred to the slider that is preloaded against the actuator. The authors carried out numerical and experimental investigations and showed that the maximum speed of the slider is 20.17 mm/s under the driving voltage of 100 $V_{p\text{-}p}$ while the driving frequency was 610 Hz with a preload force of 2.5 N.

Yang et al. reported on the piezoelectric inertial linear motion actuator featuring an arc-shaped driving tip that is driven by a multilayer piezoelectric actuator via flexible hinges [22]. Longitudinal displacements of the multilayer actuator are excited using a sawtooth electric signal and are transferred to an arc-shaped driving tip; therefore, inertial stick–slip operation is obtained. The authors conducted numerical and experimental investigations and found that the actuator is able to provide 2754 μm/s under a driving voltage of 120 V while the preload force was 5N.

Ko et al. introduced a piezoelectric linear motion actuator based on a bimorph piezoelectric disc that operates based on the inertial principle [23]. The actuator consists of a bimorph piezoelectric disc clamped in a special housing. A guidance rail with a slider is placed in the center of the disc. The actuator is excited by a sawtooth signal at the frequency equal to or close to the first out-of-plane bending mode of the bimorph disc. Displacements of the slider along the rail are obtained because of the different vibration velocities of the disc when it bends in different directions. It was shown that the actuator can provide linear speed up to 15 mm/s output force of 140 mN.

This paper represents numerical and experimental investigations of a novel inertial piezoelectric linear actuator that is based on a square cross-section-shaped rod stator. The design and operating principle of the actuator is described in Section 2. The results of numerical modeling and simulation are presented in Section 3. Prototype and experimental measurements are provided in Section 4. Finally, Section 5 concludes this work.

2. Design and Operation Principle of the Actuator

The proposed linear piezoelectric actuator consists of a square cross-section-shaped rod made of beryllium bronze, eight piezoceramic plates, a T-shaped clamping element, a guidance rail, and a slider (Figures 1 and 2). The aforementioned rod contains an asymmetric hollowed cut and T-shaped clamping element in the central zone of the rod. The cut is made with an offset from the longitudinal axis of symmetry of the rod, resulting in the formation of a slender wall. Piezoceramic plates are glued on the four surfaces of the rod while the polarization direction is pointed away from the surface. The cylindrical guidance rail is located in the center of the slender wall, perpendicular to the surface, and aligned with the transversal symmetry axis of the rod. Rail is made from fiber carbon and is used as a guidance for the slider. Finally, a T-shaped clamping element is clamped on the PCB using bolts (Figure 1). The design of the actuator and its stator are shown in Figures 1–3, respectively.

The geometrical parameters of the actuator are given in Table 1. Values of geometrical parameters were obtained during the optimization study. A detailed description of the design optimization of the stator is given in Section 3.

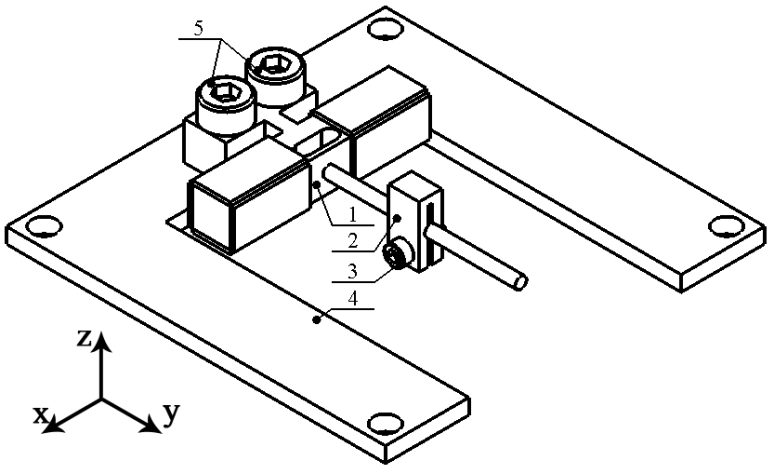

Figure 1. Design of the linear actuator: 1—stator of the actuator; 2—slider; 3—bolt for slider clamping; 4—printed circuit board; and 5—bolts for stator clamping.

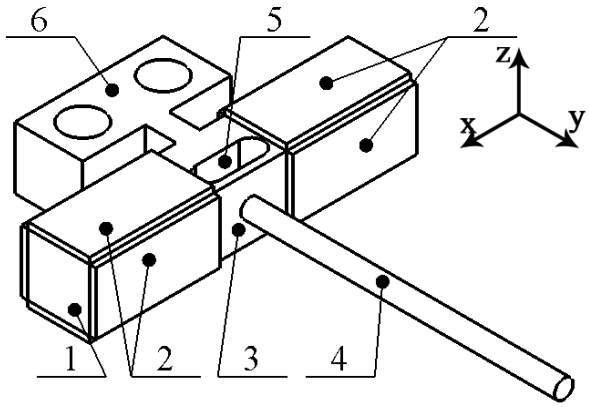

Figure 2. Design of the stator: 1—square-shaped rod; 2—piezo ceramic plates; 3—thin wall; 4—guide rail; 5—asymmetric cut; and 6—T-shaped clamping.

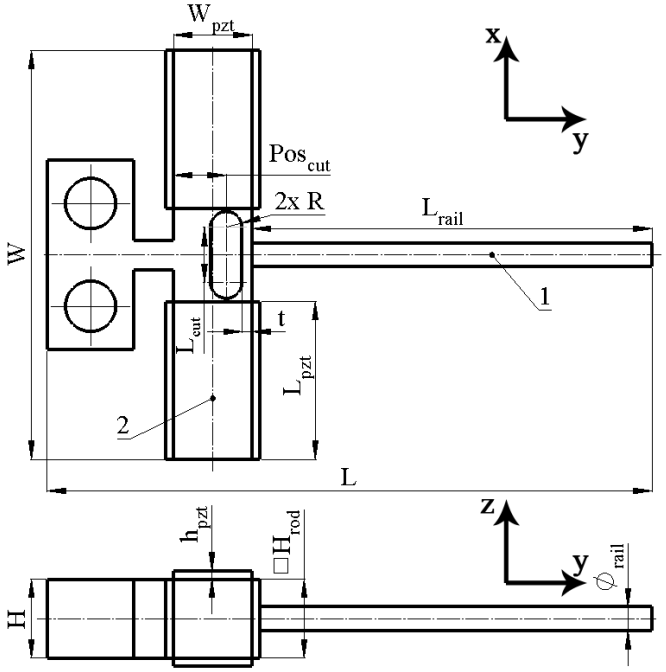

Figure 3. Sketch of the actuator; 1—horizontal axis of symmetry of actuator; 2—longitudinal axis of square rod.

Table 1. Geometrical parameters of the actuator.

Geometrical Parameter	Value	Description
L	40 mm	Length of actuator
L_{rail}	25 mm	Length of guidance rail
Pos_{cut}	3.35 mm	Position of cut
L_{cut}	3.5 mm	Length of cut
L_{pzt}	10 mm	Length of piezo ceramic plate
W	25.9 mm	Length of square-shaped rod
W_{pzt}	5 mm	Width of piezo ceramic plate
R	1 mm	Radius of cut
H	5 mm	Height of actuator
H_{rod}	5 mm	Height of square-shaped rod
h_{pzt}	0.5 mm	Thickness of piezo ceramic plates
$Ø_{rail}$	1.5 mm	Diameter of guidance rail
t	1 mm	Thickness of wall

The operation of the actuator is based on the inertial stick—slip principle. The first longitudinal vibration mode of the square cross-section rod is excited using two sawtooth waveform electric signals with a phase difference of π. The vibration mode of the first longitudinal mode is induced and generates transversal deformations in the central zone of the rod. Asymmetrical longitudinal vibrations are employed to obtain bending vibrations of the slender wall and longitudinal motion of the guidance rail. In order to obtain the linear motion of the slider, the asymmetrical motion of the rail is used.

In order to amplify the amplitude of the transversal vibrations in the nodal zone of the square cross-section rod, the hollowed cut is used. The position of the cut is selected in such a way that it forms the thin wall that produces bending vibrations when longitudinal vibrations of the rod are excited. Moreover, the asymmetrical cut and T-shaped clamping ensure asymmetrical stiffness of the square rod, and as a result, bending in-plane deformations of square cross-section rods are induced, which increases displacement amplitudes as well as creates the possibility of control linear motion.

Two sawtooth electric signals with a phase difference of π and frequency close to the resonance frequency of the first longitudinal deformation mode of the square cross-section-shaped rod are used for actuator driving. Eight piezo ceramic plates are divided into three groups and ensure excitation of the first longitudinal vibration mode and bending in-plane deformations of the rod. The groups of the piezoceramic plates and the actuator excitation schematic, are shown in Figure 4. The following excitation regime is used, i.e., the first group of piezo ceramic plates is used to excite the first longitudinal vibrations (Figures 2 and 4) when a sawtooth electric signal is applied. The other two groups of electrodes are used to induce bending vibrations, control motion direction of the slider, and increase in-plane bending deformations of the rod (Figures 3 and 4). These groups are driven by two sawtooth signals with the phase difference of π. Therefore, by such excitation schematics, longitudinal vibration mode is excited and ensures output force and linear motion speed while, in plane, bending deformations, which appear due asymmetrical design of the stator, are enlarged by two groups of piezo ceramic plates. The motion direction of the slider is changed via swapping of signals between groups of the electrodes used for inducing bending deformations.

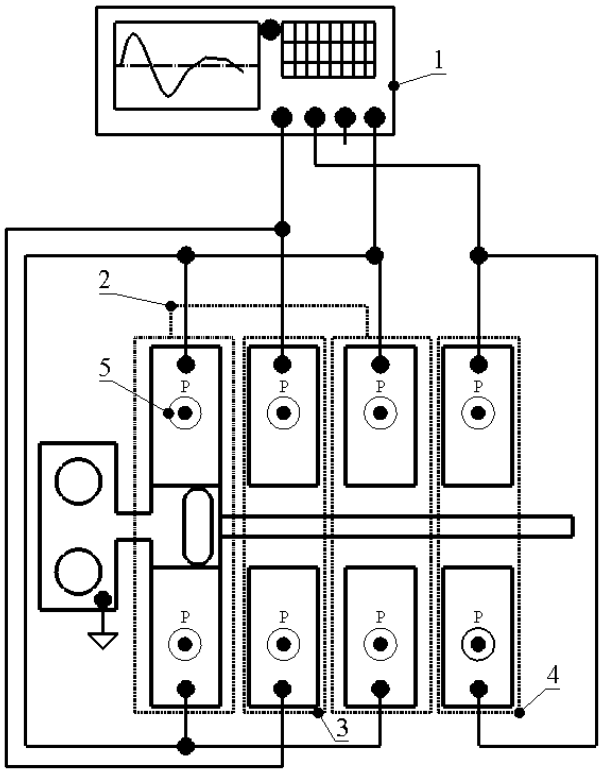

Figure 4. Excitation schematics of actuator; 1—signal generator; 2—group of piezo ceramic plates used to excite longitudinal vibrations; 3—the first group of piezo ceramic used to excite bending vibrations; 4—the second group of piezo ceramic plates used to excite bending vibrations; 5—polarization direction of piezo ceramic plates.

3. Numerical Investigation of the Actuator

Numerical investigations were performed in order to confirm the operation principle and indicate the mechanical and electromechanical characteristics of the actuator. Also, an optimization study was performed to obtain optimal geometrical and mechanical characteristics of the actuator. The Finite Element Model (FEM) was built using the COMSOL Multiphysics software with strict respect to the actuator geometry, which is represented in Figure 2. Moreover, the boundary conditions were established as follows: the T-shaped clamping was rigidly fixed. Electrical boundary conditions were set with respect to the schematics shown in Figure 4. Finally, the material properties were included in the model.

The C17200 beryllium bronze was used for the rod and T-shaped clamping element, the properties of NCE81 (CTS Corp, USA) hard piezo ceramic were applied to piezoceramic plates, and the carbon fiber characteristics for the guide guidance rail (Table 2).

Table 2. Properties of the materials.

Material Properties	C17200 Beryllium Bronze	CTS Corp NCE81	Carbon Fiber
Density, [kg/m^3]	8360	7730	1600
Young's modulus, [N/m^2]	13.1×10^{10}	-	7.1×10^{10}
Poisson's coefficient	0.34	0.32	0.15
Isotropic structural loss factor	0.02	-	0.1
Relative dielectric constant	-	$\varepsilon_{33}{}^{T}/\varepsilon_0 = 1020$	-
Elastic compliance coefficient [10^{-12} m^2/N]	-	$S_{11}{}^{E} = 16.00$ $S_{33}{}^{E} = 17.00$	-
Piezoelectric charge constant d_{33} [10^{-12} m/V]	-	255	-
Piezoelectric constant d_{31} [10^{-12} m/V]	-	-100	-
Electromechanical coupling factors	-	$k_p = 0.55$ $k_{31} = 0.30$ $k_{33} = 0.69$ $k_t = 0.47$	

The first step of the numerical investigation was dedicated to finding the optimal geometric parameters of the actuator. For this purpose, a frequency domain study was made in the frequency range of 35 kHz to 75 kHz with a step of 5 Hz, while the excitation signal was set to 100 $V_{p\text{-}p}$. Optimization of the actuator was performed with the goal of maximizing displacement amplitudes of the guidance rail in the y direction by changing the geometrical parameters of the asymmetrical cut and the length of the square cross-section-shaped rod. The amplification ratio between the output and input displacement amplitudes $\frac{u_y}{u_x}$ was used as optimization criteria. The description of the optimization problem is as follows:

$$\underset{L_{cut}, R, W}{max} \left(\frac{u_y}{u_x}(L_{cut}, R, W) \right); \tag{1}$$

subjected to

$$L_{cut}^{min} \leq L_{cut} \leq L_{cut}^{max}; \tag{2}$$

$$R_{min} \leq R \leq R_{max}; \tag{3}$$

$$W = L_{cut} + 2R + 2L_{pzt}; \tag{4}$$

here, u_x is the longitudinal displacement of the rod; u_y is the longitudinal displacement amplitude of the guidance rail in the y direction; L_{cut} is the length of the hollowed cut excluding the radius of endings; R is the radius of hollowed cut endings; W is the total length of the squared-shaped rod; L_{cut}^{min} is the lowest value of asymmetrical cut length; L_{cut}^{max} is the highest value of asymmetrical cut length; R_{min} is the lowest value of the radius of asymmetrical cut endings; and R_{max} is the highest value of the radius of asymmetrical cut endings. In order to carry out the linear optimization study, the values of L_{cut}^{min} and L_{cut}^{max} were set to 3 mm and 7 mm with an increment step of 0.5 mm. R_{min} and R_{max} were set to 0.5 mm and 1.75 mm with an increment step of 0.25 mm was used. Equation (4) shows that the total length of the rod (W) depends on the length of piezo ceramic plates, radius R, and length L_{cut}. It means that the total length of the rod will be changed at every step of calculations. The results of the study are shown in Figure 5.

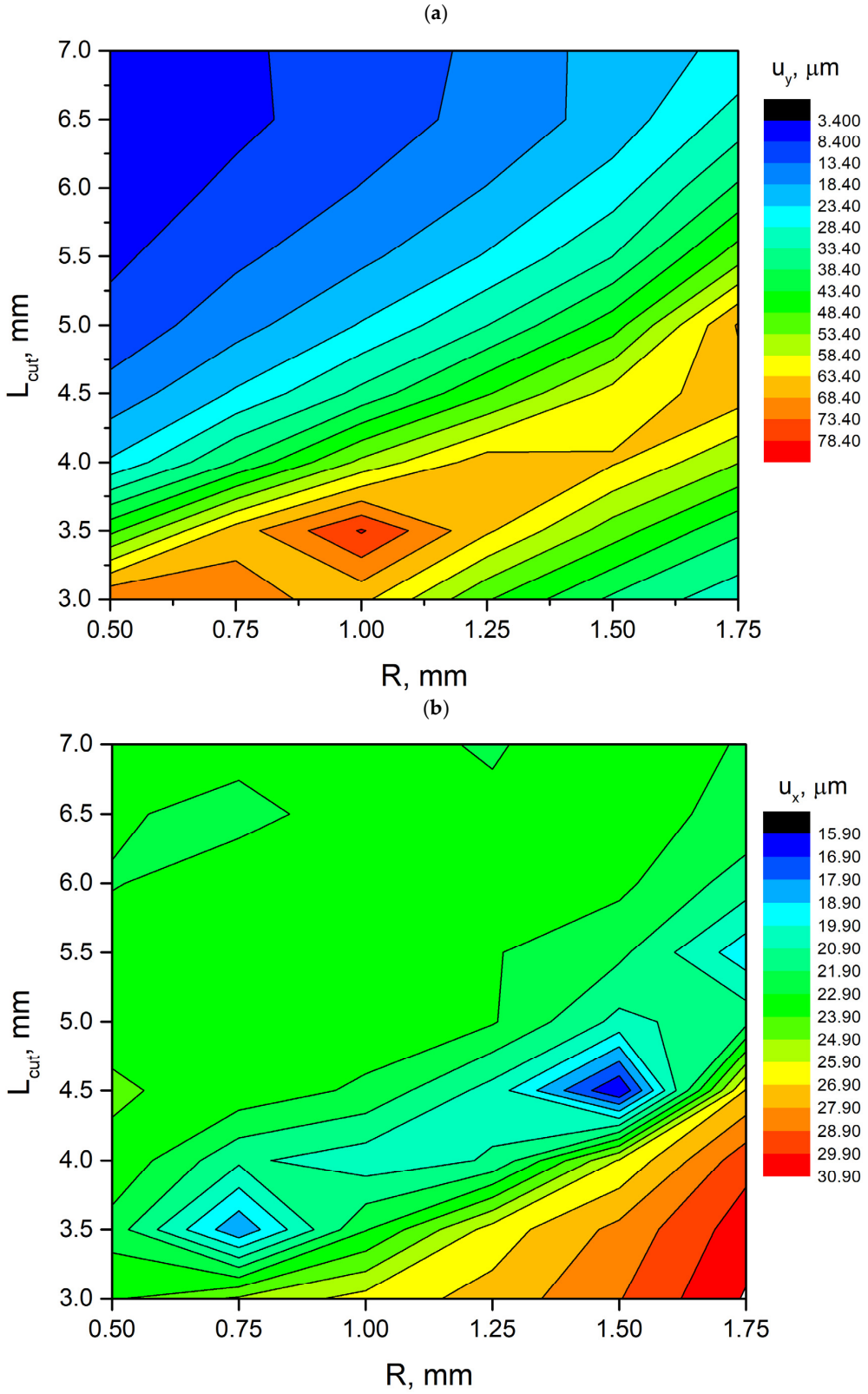

Figure 5. Displacement amplitudes of the actuator in the first longitudinal vibration mode while different geometrical parameters are applied: (**a**) longitudinal displacement of the guidance rail and (**b**) longitudinal displacement amplitude of the square-shaped rod.

Analyzing the results, it can be found that the highest longitudinal displacement amplitude of the guide rail (u_y) was obtained, while L_{cut} was equal to 3.5 mm and R was

equal to 1 mm and reached 76.4 µm. On the other hand, as Figure 5b shows, the average longitudinal displacement of rod (u_x) amplitudes is around 23.5 µm. In addition, it can be found that the u_x values have an almost even distribution among all possible combinations of geometrical parameters. Therefore, it can be stated that optimal geometrical parameters of the actuator were obtained. However, considering that the actuator design foresees amplification of displacements of the first longitudinal vibration mode, the ratio $\frac{u_y}{u_x}$ was calculated in the full range of L_{cut} and R parameters. The results are given in Figure 6.

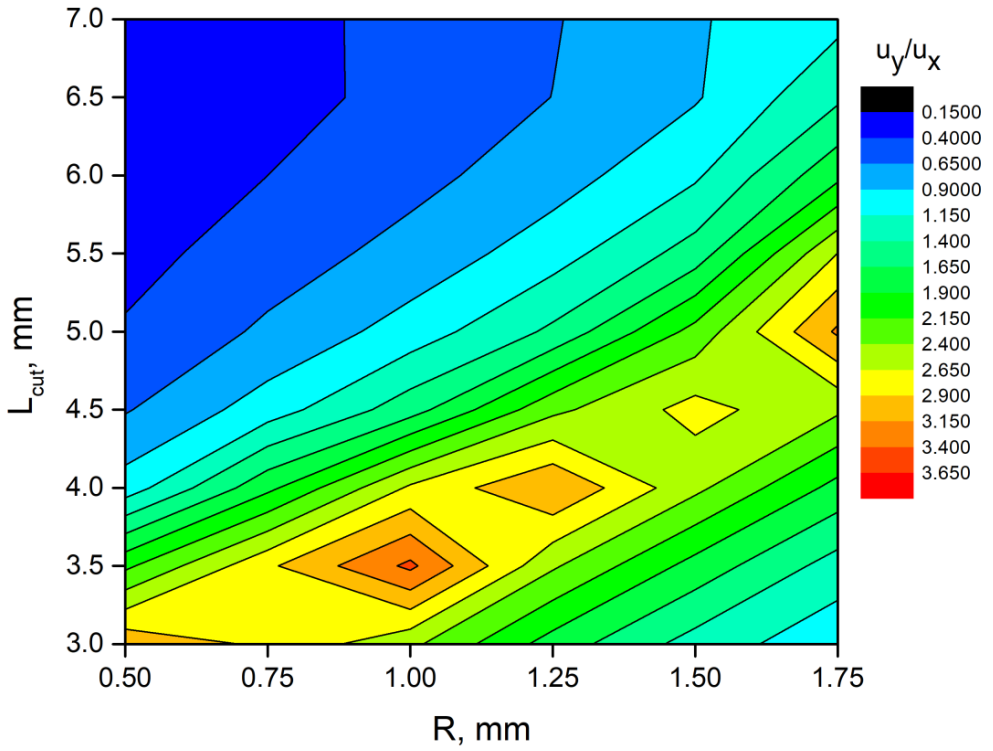

Figure 6. Amplification ratio between output and input displacement amplitudes at different geometrical parameters.

The best ratio $\frac{u_y}{u_x}$ value of 3.45 was obtained when L_{cut} was 3.5 mm, and R was 1 mm. It means that the vibration amplitude of the guidance rail was amplified 3.45 times compared to the amplitude of the first longitudinal vibrations of the square-shaped rod. More detailed results of the actuator length (W) calculations at the resonance frequencies of the first longitudinal vibration mode are shown in Figure 7.

It can be seen that the resonance frequency of 59.12 kHz was obtained when the optimal values of L_{cut} and R were calculated. This frequency can be called the operating frequency of the actuator. In addition, Figure 7b shows the lengths (W) of the rod while different geometric parameters were applied. As it can be found, it has linear behavior while its value was directly related to L_{cut} and R and calculated according to Equation (4). Therefore, considering the plot, the length (W) of the square-shaped rod is 29.5 mm. Finally, to fully represent the results of the calculations, a summary of the results was made (Table 3).

The geometric parameters given in Table 3 will be used for further numerical investigations that will focus on the confirmation and indication of the mechanical and electromechanical characteristics of the actuator.

Table 3. Optimal parameters of the actuator.

Parameter	L_{cut}	R	u_x	u_y	u_y/u_x	f_r	W
Value	3.5 mm	1 mm	22.86 µm	78.9 µm	3.45	59.12 kHz	29.5 mm

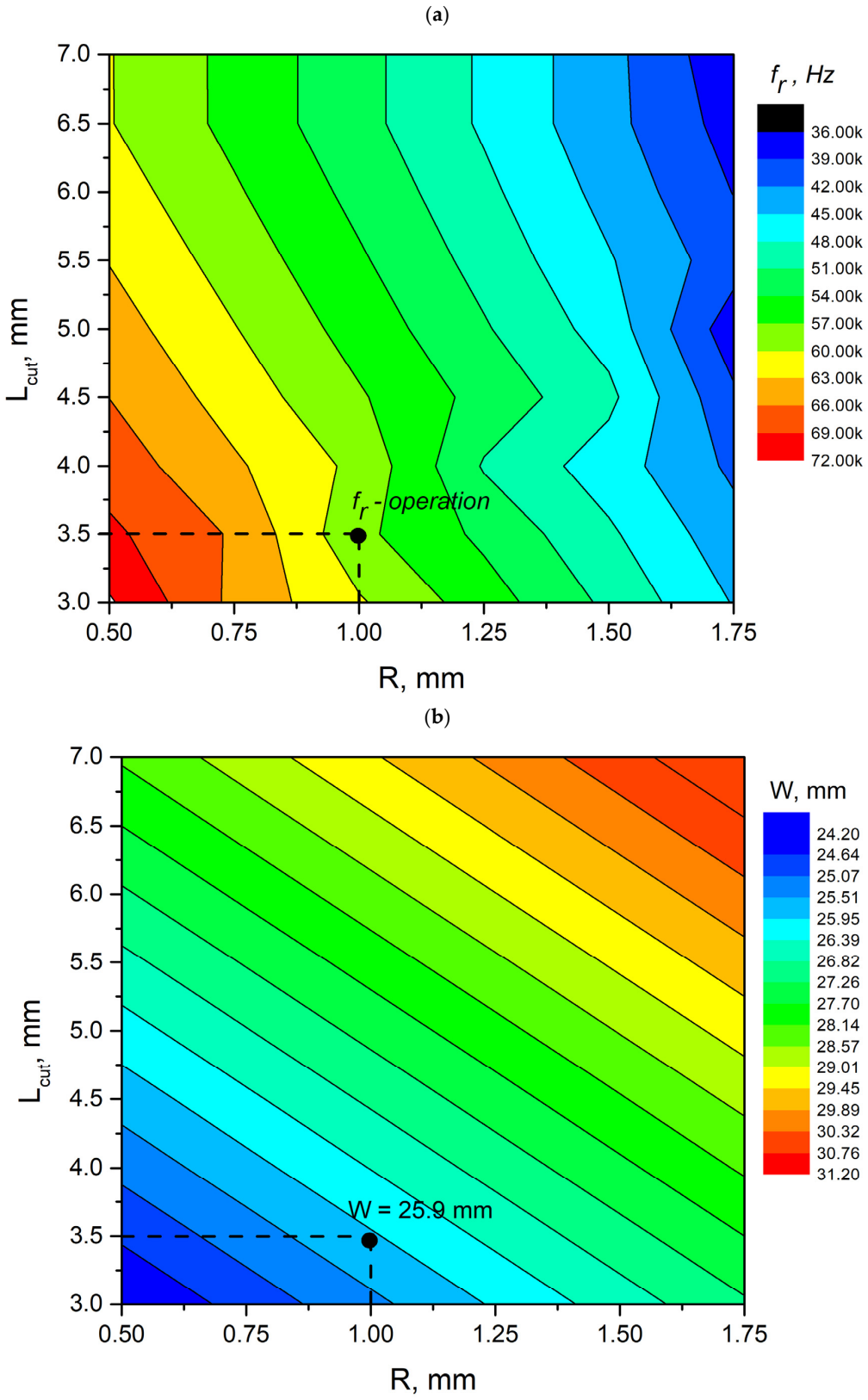

Figure 7. Plots of resonance frequencies and rod lengths are used while different geometrical parameters are used: (**a**) resonant frequencies of the first longitudinal vibration mode; (**b**) lengths of square-shaped rod.

The next step of the numerical investigation was dedicated to modal analysis of the actuator. In order to carry out this study, the geometric parameters given in Table 3 were applied to the numerical model of the actuator. The goal of the analysis was to indicate the

modal shape of the actuator and to confirm the presence of bending deformations, which are inducted by the asymmetric design. The results of the modal analysis are given in Figure 8. As can be seen, the modal shape of the actuator confirms its operation in the first longitudinal vibration mode of the square-shaped rod. In addition, it can be found that despite longitudinal vibrations of the rod, it also has bending deformations, which confirms the assumption that the asymmetrical design of the actuator, the usage of cut and T-shaped clamping, enables this type of vibration. Finally, the modal shape shows that the thin wall operates as a mechanical displacement amplifier and allows to increase in displacement amplitudes generated by longitudinal vibrations.

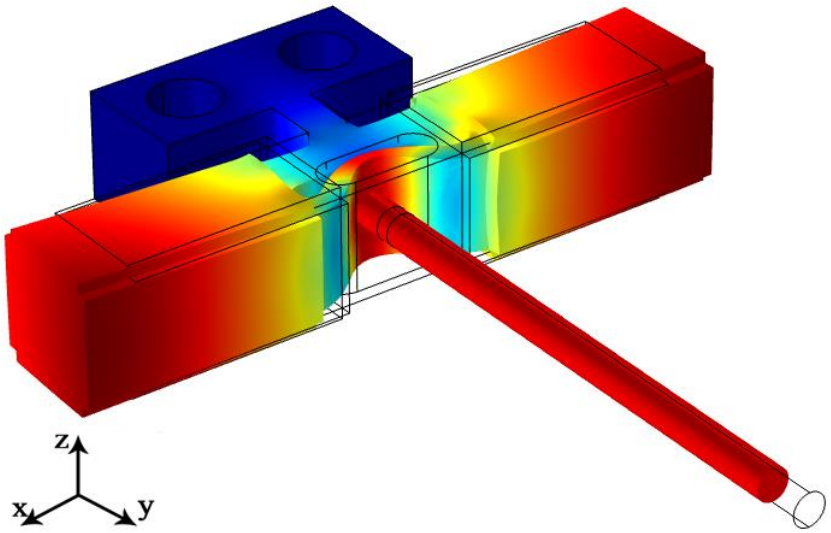

Figure 8. The modal shape of the actuator at 59.72 kHz.

Impedance and phase frequency characteristics of the actuator were analyzed as well. For this purpose, a frequency domain study for a range from 59.7 to 60 kHz with the step of 5Hz was set, while mechanical and electrical boundary conditions were set as in previous studies. The results of the calculations are shown in Figure 9.

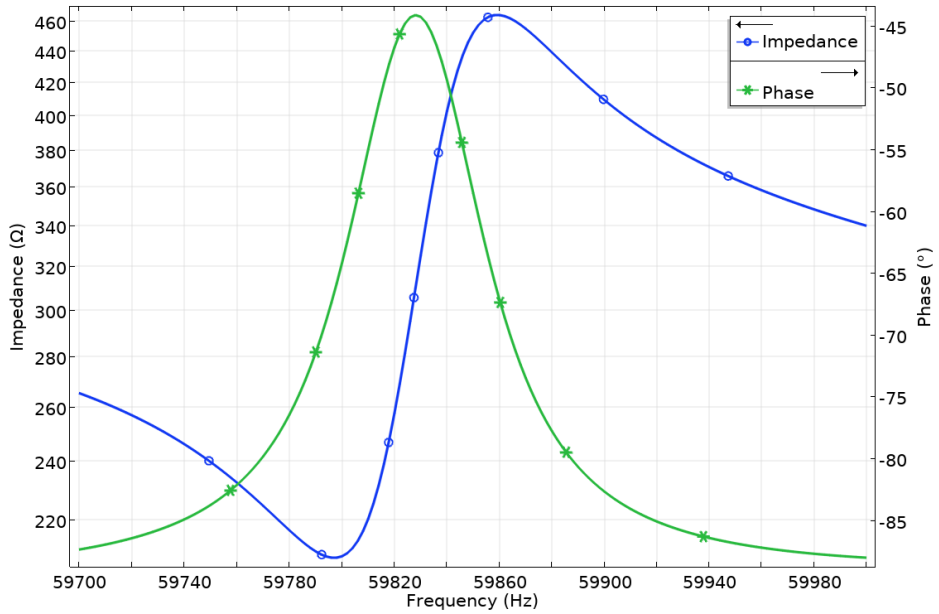

Figure 9. Impedance and phase—frequency characteristics of the actuator.

As can be found in Figure 9, the resonance frequency of the actuator was 59.82 kHz. A slight mismatch between resonant values obtained by modal analysis and harmonic response studies was caused by minor differences in the mesh as well as in discreet steps used in the frequency domain study. The electromechanical effective coupling k_{eff} of the actuator was calculated (Equation (5)) and reached a value of 0.045.

$$\frac{k_{eff}^2}{1-k_{eff}^2} = \frac{f_a^2 - f_r^2}{f_r^2} \tag{5}$$

here, k_{eff} is electromechanical effective coupling; f_a is antiresonance frequency; and f_r is resonance frequency.

The time domain study was performed to indicate the operation sequence of the actuator and to confirm the operation principle. The study lasted for one period (T) of operation frequency. Mechanical boundary conditions were set as in the previous case, while the excitation signal was set to a sawtooth-shaped signal. The operation sequence of the actuator is shown in Figure 10 and confirms the inertial operation principle of the actuator. It can be found that longitudinal displacements of the square rod are directly related to excitation signal waveform and lead to asymmetrical displacements of the rod and cylindrical guidance rail. Also, it can be noticed that displacements of the rod, despite longitudinal deformations, contain bending in-plane displacements that are inducted because of the asymmetrical design of the actuator. Finally, it can be found that the thin wall is bent by two opposite forces that are created by longitudinal deformations of the rod.

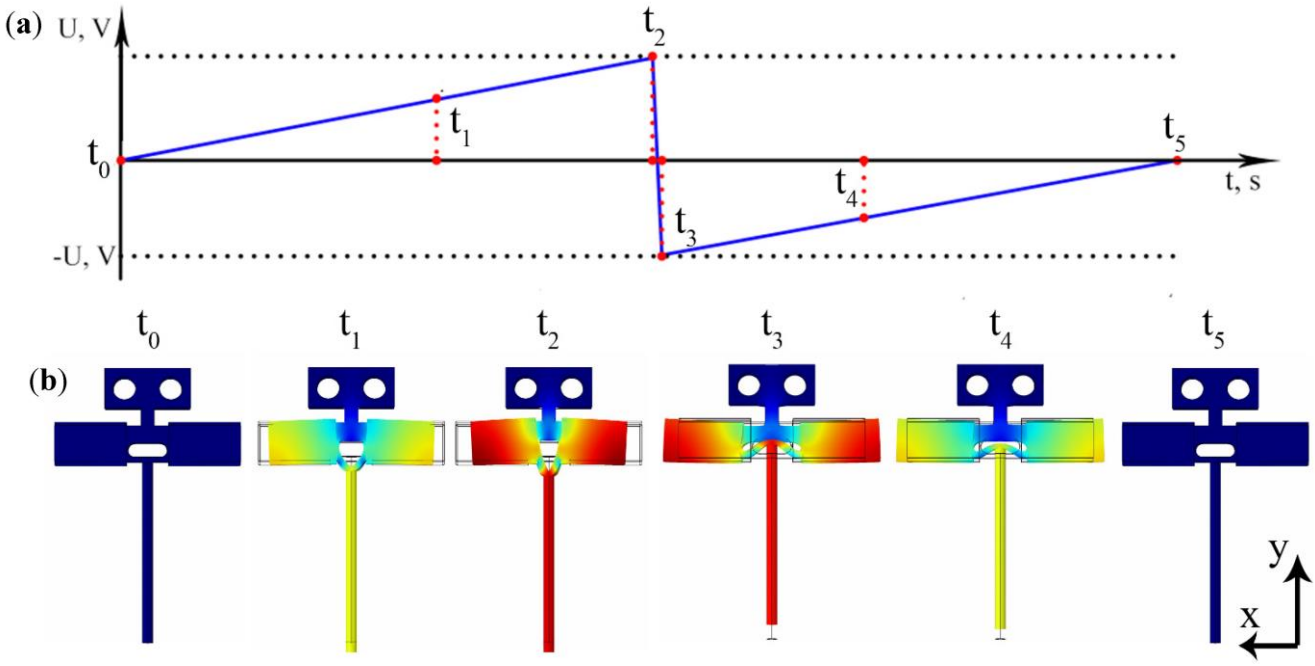

Figure 10. The operation sequence of the actuator: (**a**) sawtooth excitation signal; (**b**) sequence of actuator motions.

The numerical study was established with the objective of indicating the displacements and amplification characteristics of the actuator at different amplitudes of the excitation signal. To carry out this study, the frequency range was set from 59.4 to 60 kHz with a step of 2 Hz while the amplitude of the excitation signal changes from 40 $V_{p\text{-}p}$ to 200 $V_{p\text{-}p}$ with an increment step of 20 $V_{p\text{-}p}$. The results of the simulation are given in Figure 11.

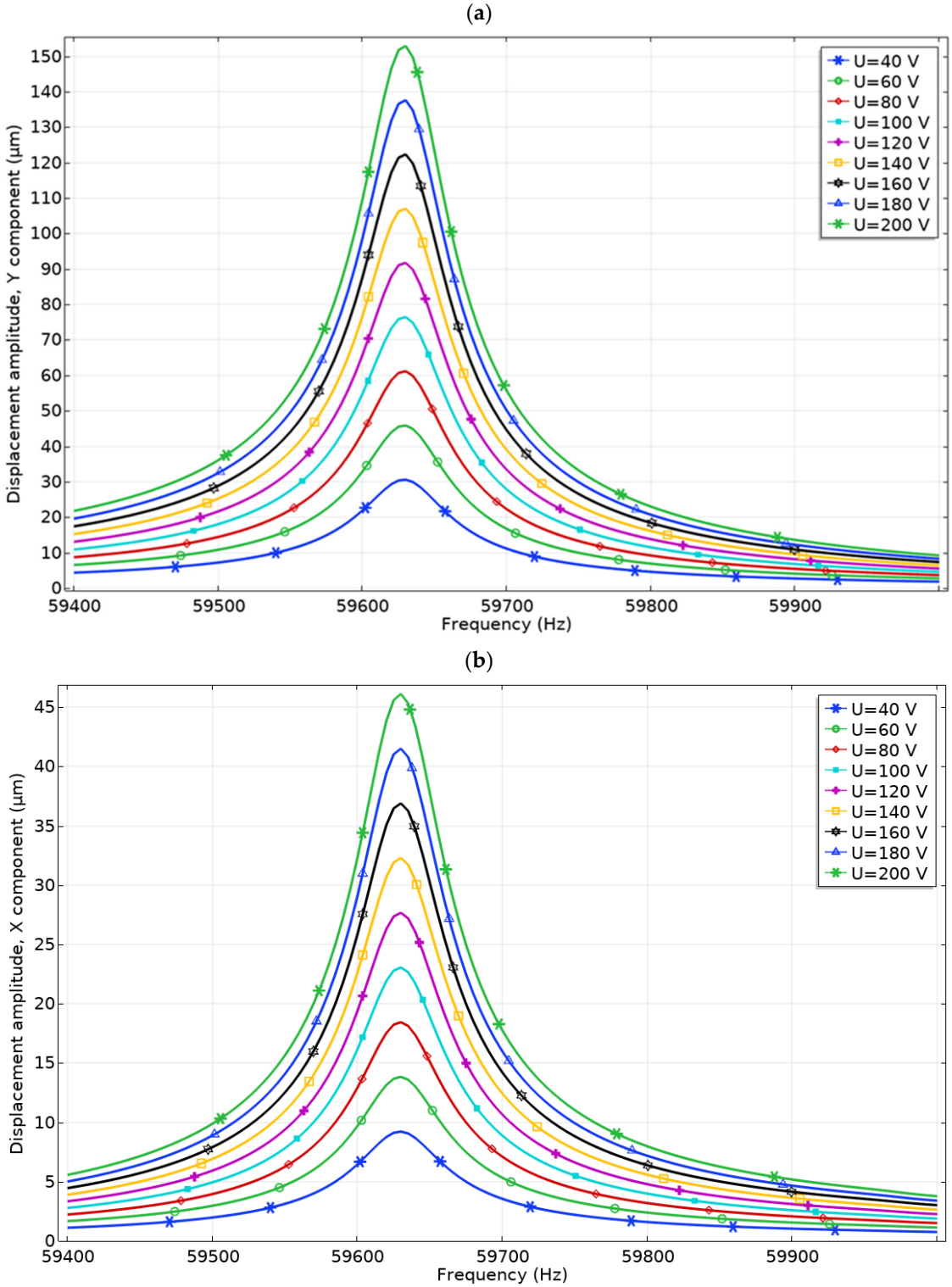

Figure 11. Displacement amplitudes of the actuator; (**a**) displacements of cylindrical guidance rail in the *y* direction; (**b**) displacements of square-shaped rod in the *x* direction.

It can be seen that the displacement amplitudes of the cylindrical guidance rail in the *y* direction depend on the amplitude of the excitation signal. The lowest displacement amplitude of the rail was obtained at 40 $V_{p\text{-}p}$ and reached 30.5 μm or 762.5 nm/$V_{p\text{-}p}$. The highest rail displacement amplitude was obtained at 200 $V_{p\text{-}p}$ and reached 152.9 μm or 764.5 nm/Vp-p. On the other hand, the displacement amplitudes of a square cross-section-shaped rod in the *x* direction when the voltage of 40 $V_{p\text{-}p}$ and 200 $V_{p\text{-}p}$ is applied are

9.2 μm and 46.12 μm or 230 nm/$V_{p\text{-}p}$ and 231 nm/$V_{p\text{-}p}$, respectively. Moreover, it can be found that the amplification ratio of the square-shaped rod displacement is approximately 3.31 times at the whole range of excitation signal amplitudes. These results show that the actuator can provide stable and well-predictable output displacements and a wide range of excitation signal amplitudes. Stable displacement characteristics ensure the possibility of using flexible and simple excitation systems for actuator control and driving.

4. Experimental Investigation of the Actuator

Experimental investigations were carried out to validate the results of numerical investigations. The actuator prototype was made with strict respect to the geometrical parameters and material properties indicated in the section related to numerical investigations (Figure 12).

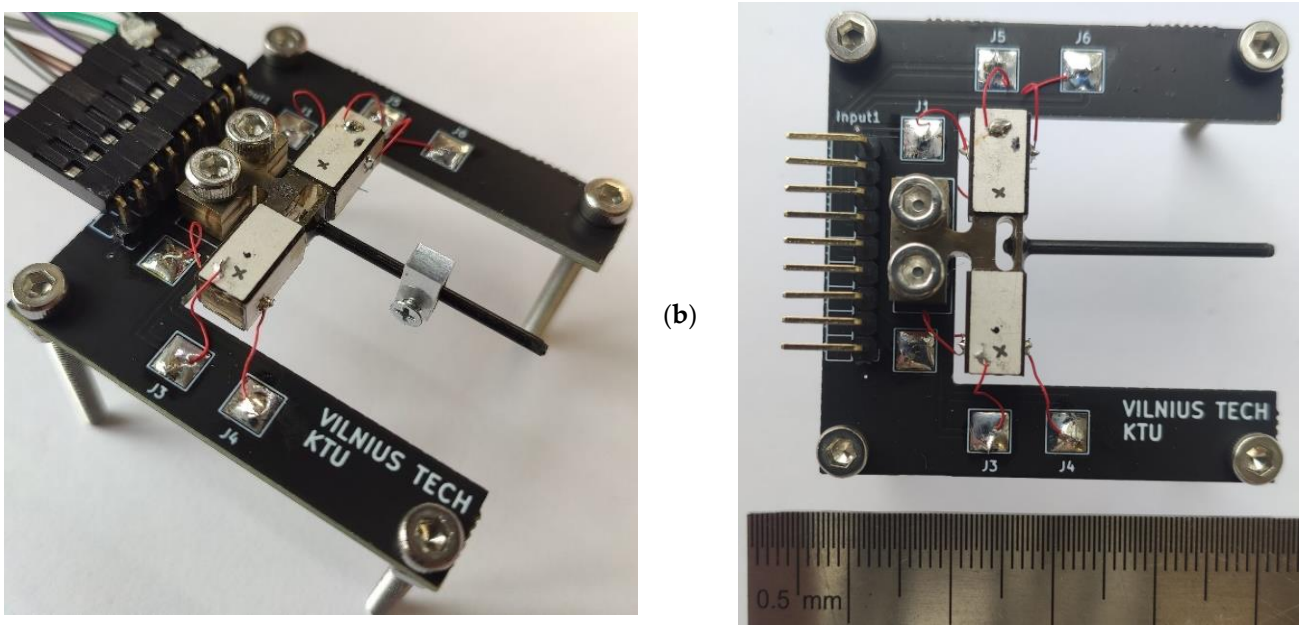

Figure 12. Prototype of the actuator: (**a**) side view; (**b**) top view.

Firstly, impedance and phase characteristics were measured in the frequency domain. Hewlett-Packard 4294A impedance analyzer (Hewlett-Packard, CA, USA) was used. The results of the measurements are given in Figure 13.

Results showed that the resonant frequency of the first longitudinal vibration mode is obtained at 59.45 kHz. The difference between the calculated and measured values is less than 1%, while the impedance values have notable differences. In addition, the electromechanical effective coupling coefficient k_{eff} was found and equaled 0.061 (Equation (5)). Differences in k_{eff} values occur due to differences in clamping and the glue layer that were neglected in the numerical model and minor mismatches in material characteristics, manufacturing, and assembly errors. However, the results of experimental and numerical investigations are in good agreement, and further experimental investigations can be performed.

Linear motion speeds of the slider were measured when different loads and excitation signal amplitudes were applied. For this purpose, an experimental setup was assembled (Figure 14).

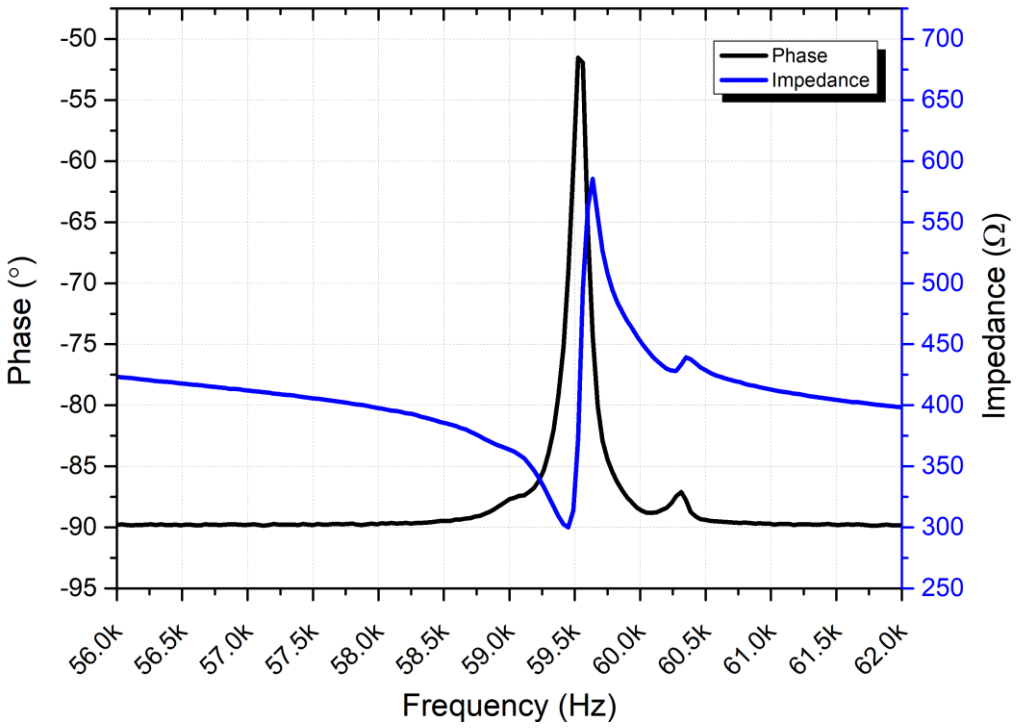

Figure 13. Impedance and phase frequency characteristics of the actuator.

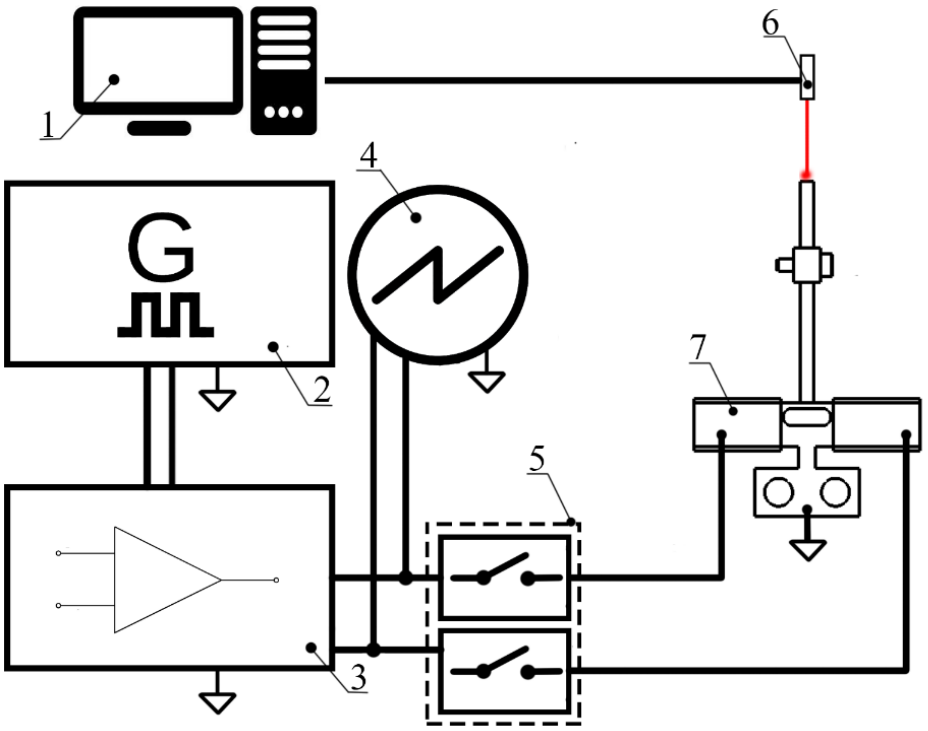

Figure 14. Schematics of the experimental setup: 1—computer; 2—signal generator; 3—power amplifier; 4—oscilloscope; 5—signal junction box; 6—displacement sensor; and 7—prototype of actuator.

The experimental setup included a computer, function generator WW5064 (Tabor Electronics, Nesher, Israel), a power amplifier PD200 × 4 (Piezo Drive, Shortland, Australia), an oscilloscope DL2000 (Yokogawa, Tokyo, Japan), a displacement sensor ILD 2300 (Micro-Epsilon, Ortenburg, Germany) and a custom-made signal junction box for control of

motion direction. The results of the speed measurements are shown in Figure 15 while Supplementary Material Video S1 represents operation of the actuator.

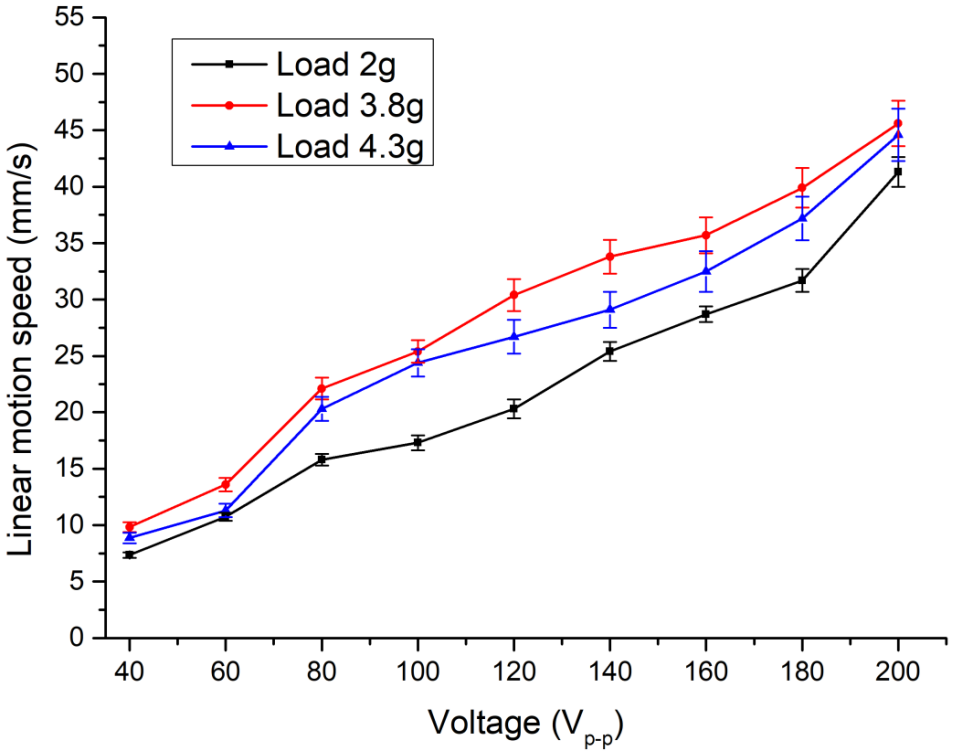

Figure 15. Motion speed characteristics under different loads and excitation signal amplitudes.

As can be found in Figure 15, the highest linear motion speed of 45.6 mm/s was obtained at a voltage of 200 V_{p-p} while the load was 3.8 g. The motion speed per voltage ratio was 0.228 mm/s/V_{p-p}. On the other hand, at the same load conditions and excitation signal amplitude of 40 V_{p-p}, the lowest linear speed reached 9.83 mm/s or 0.245 mm/s/V_{p-p}. The lowest linear motion speeds were obtained when a load of 2 g was applied, and the voltage was 200 V_{p-p}. The linear speed of the slider reached 41.3 mm/s or 0.206 mm/s/V_{p-p}, while the voltage of 40 V_{p-p} speed reached 7.35 mm/s or 0.184 mm/s/V_{p-p}. Therefore, it can be stated that an actuator can provide stable and well-predictable linear motion speed at a wide range of voltage and load values.

The next step of investigations was dedicated to measuring output force at different excitation voltages and loads. The results of the measurements are shown in Figure 16.

The highest output force of 115.4 mN was obtained at the voltage of 200 V_{p-p} while the load of 3.8 g was applied. The force per voltage ratio reached 577 μN/V_{p-p}. The lowest output force was obtained under the same load condition while the excitation signal was set at 40 V_{p-p} and reached 31.6 mN or 790 μN/V_{p-p}. In addition, it can be found that the lowest output force characteristics were obtained at a load of 2 g. The force values of 91.3 mN or 456.5 μN/V_{p-p} were obtained at 200 V_{p-p}. When the voltage was set to 40 V_{p-p}, the force values reached 27.9 mN or 697.5 μN/V_{p-p}. Despite minor fluctuations in output force values, it can be concluded that the actuator can provide stable output forces at a wide range of excitation signal amplitudes and different loads.

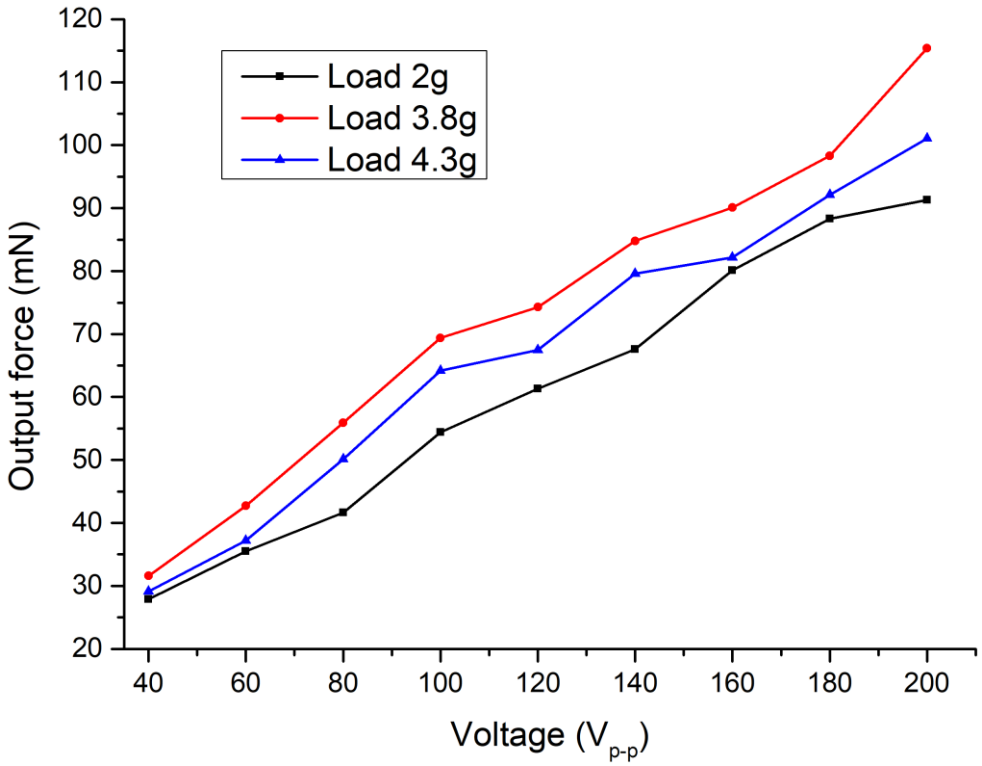

Figure 16. Output force characteristics at different loads and excitation signal amplitudes.

5. Conclusions

The novel design of the piezoelectric linear motion actuator was proposed and investigated. The operation principle of the actuator is based on the inertial stick-slip principle, which is inducted by the first longitudinal vibration mode of the square cross-section-shaped rod. In addition, the asymmetrical design of the actuator, formed by asymmetric cut and clamping, ensures an additional bending deformation of the rod, which leads to an increase in dynamic characteristics. Moreover, a thin wall, formed by an asymmetric cut, ensures that longitudinal vibrations are transferred to the cylindrical guidance rail and are amplified. Optimal geometric parameters were obtained that allowed an increase in vibration amplitudes of the guidance rail significantly and achieved an amplification ratio up to 3.45. Results of modal and harmonic response analysis have shown that the actuator operation frequency is 59.82 kHz. Numerical simulation also confirmed that it is possible to obtain longitudinal vibrations of the guidance rod when the first longitudinal vibration mode or the rod is excited. Experimental investigations have shown that the highest linear motion speed of 45.6 mm/s was obtained when the voltage of 200 V_{p-p} was applied at the load of 3.8 g. The results of the thrust force measurements showed that the actuator can provide up to 115.4 mN of output force while the excitation voltage of 200 V_{p-p} was applied.

Supplementary Materials: The following supporting information can be downloaded at https://www.mdpi.com/article/10.3390/act12100379/s1, Video S1: Video of the operation of the actuator.

Author Contributions: Conceptualization, A.Č., D.M. and V.J.; methodology, A.Č. and V.B.; validation, A.Č. and D.M., formal analysis, V.J. and D.D.; investigation, A.Č. and V.B.; data curation, A.Č. and D.D.; writing—original draft preparation, A.Č. and V.J.; writing—review and editing, D.M.; visualization, A.Č. and D.M.; supervision, V.J.; project administration, A.Č. and V.J. All authors have read and agreed to the published version of the manuscript.

Funding: This research was funded by the Research Council of Lithuania according to the activity "Postdoctoral fellowships studies" under funding agreement No. S–PD–22–18.

Data Availability Statement: Not applicable.

Conflicts of Interest: The authors declare no conflict of interest.

References

1. Mohith, S.; Upadhya, R.A.; Navin, K.P.; Kulkarni, S.M.; Rao, M. Recent Trends in Piezoelectric Actuators for Precision Motion and Their Applications: A Review. *Smart Mater. Struct.* **2021**, *30*, 013002. [CrossRef]
2. Ahmed, S.A.; Mohsin, M.; Zubair, A.; Syed, M. Survey and Technological Analysis of Laser and Its Defense Applications. *Def. Technol.* **2021**, *17*, 583–592. [CrossRef]
3. Gao, X.; Yang, J.; Wu, J.; Xin, X.; Li, Z.; Yuan, X.; Shen, X.; Dong, S. Piezoelectric Actuators and Motors: Materials, Designs, and Applications. *Adv. Mater. Technol.* **2019**, *5*, 1900716. [CrossRef]
4. Ley, P.P.; Knöchelmann, M.; Kloppenburg, G.; Lachmayer, R. Development Methodology for Optomechatronic Systems Using the Example of a High-Resolution Projection Module. *Proc. Des. Soc. Int. Conf. Eng. Des.* **2019**, *2019*, 2547–2556. [CrossRef]
5. Khalid, S.; Khan, F.; Ullah, B.; Ahmad, Z.; Akbar, S. Review of Moving Magnet Linear Oscillating Actuators for Linear Compressor Application. *World J. Eng.* **2022**, *20*, 846–856. [CrossRef]
6. Logozzo, S.; Valigi, M.C.; Canella, G. Advances in Optomechatronics: An Automated Tilt-Rotational 3D Scanner for High-Quality Reconstructions. *Photonics* **2018**, *5*, 42. [CrossRef]
7. Dalbins, J.; Allaje, K.; Iakubivskyi, I.; Kivastik, J.; Komarovskis, R.O.; Plans, M.; Sunter, I.; Teras, H.; Ehrpais, H.; Ilbis, E.; et al. ESTCube-2: The Experience of Developing a Highly Integrated CubeSat Platform. In Proceedings of the 2022 IEEE Aerospace Conference (AERO), Big Sky, MT, USA, 5–12 March 2022. [CrossRef]
8. Tian, X.; Liu, Y.; Deng, J.; Wang, L.; Chen, W. A Review on Piezoelectric Ultrasonic Motors for the Past Decade: Classification, Operating Principle, Performance, and Future Work Perspectives. *Sens. Actuators A Phys.* **2020**, *306*, 111971. [CrossRef]
9. Li, J.; Huang, H.; Morita, T. Stepping Piezoelectric Actuators with Large Working Stroke for Nano-Positioning Systems: A Review. *Sens. Actuators A Phys.* **2019**, *292*, 39–51. [CrossRef]
10. Jin, H.; Gao, X.; Ren, K.; Liu, J.; Qiao, L.; Liu, M.; Chen, W.; He, Y.; Dong, S.; Shuxiang, X.; et al. Review on Piezoelectric Actuators Based on High-Performance Piezoelectric Materials. *IEEE Trans. Ultrason. Ferroelectr. Freq. Control* **2022**, *69*, 3057–3069. [CrossRef]
11. Mukhopadhyay, S.; Behera, B.; Kumar, J. A Brief Review on the Recent Evolution in Piezoelectric Linear Ultrasonic Motors. *Eng. Res. Express* **2021**, *3*, 042003. [CrossRef]
12. Do, X.P.; Choi, S.B. A State-of-the-Art on Smart Materials Actuators over the Last Decade: Control Aspects for Diverse Applications. *Smart Mater. Struct.* **2022**, *31*, 053001. [CrossRef]
13. Wang, L.; Chen, W.; Liu, J.; Deng, J.; Liu, Y. A Review of Recent Studies on Non-Resonant Piezoelectric Actuators. *Mech. Syst. Signal Process.* **2019**, *133*, 106254. [CrossRef]
14. Ryndzionek, R.; Sienkiewicz, L. A Review of Recent Advances in the Single- and Multi-Degree-of-Freedom Ultrasonic Piezoelectric Motors. *Ultrasonics* **2021**, *116*, 106471. [CrossRef] [PubMed]
15. Mashimo, T.; Toyama, S. Rotary-Linear Piezoelectric Actuator Using a Single Stator. *IEEE Trans. Ultrason. Ferroelectr. Freq. Control* **2009**, *56*, 114–120. [CrossRef]
16. Ryndzionek, R.; Sienkiewicz, L.; Michna, M.; Chodnicki, M. Design Evolution of the Ultrasonic Piezoelectric Motor Using Three Rotating Mode Actuators. *IEEE Access* **2021**, *9*, 79416–79423. [CrossRef]
17. Li, Z.; Wang, Z.; Zhao, L.; Guo, P. Characteristic Analysis and Experimental Study of Spherical Ultrasonic Motor with Multi-Degree-of-Freedom. *J. Appl. Sci. Eng.* **2020**, *23*, 619–626. [CrossRef]
18. Spanner, K.; Koc, B. Piezoelectric Motors, an Overview. *Actuators* **2016**, *5*, 6. [CrossRef]
19. Hunstig, M. Piezoelectric Inertia Motors-A Critical Review of History, Concepts, Design, Applications, and Perspectives. *Actuators* **2017**, *6*, 7. [CrossRef]
20. Koc, B.; Delibas, B. Impact Force Analysis in Inertia-Type Piezoelectric Motors. *Actuators* **2023**, *12*, 52. [CrossRef]
21. Lu, X.; Gao, Q.; Li, Y.; Yu, Y.; Zhang, X.; Qiao, G.; Cheng, T. A Linear Piezoelectric Stick-Slip Actuator via Triangular Displacement Amplification Mechanism. *IEEE Access* **2020**, *8*, 6515–6522. [CrossRef]
22. Yang, Z.; Zhou, X.; Huang, H. Design, Analysis and Experiments of a Stick-Slip Piezoelectric Actuator Working under the Self-Deformation Mode. *Smart Mater. Struct.* **2022**, *31*, 105010. [CrossRef]
23. Ko, H.; Lee, K.; Yoo, K.; Kang, C.; Kim, S.; Yoon, S. Analysis of Tiny Piezoelectric Ultrasonic Linear Motor. *Jpn. J. Appl. Phys.* **2006**, *45*, 4782–4786. [CrossRef]

Disclaimer/Publisher's Note: The statements, opinions and data contained in all publications are solely those of the individual author(s) and contributor(s) and not of MDPI and/or the editor(s). MDPI and/or the editor(s) disclaim responsibility for any injury to people or property resulting from any ideas, methods, instructions or products referred to in the content.